



Gravity-induced double encapsulation of liquids using granular rafts

Alireza Hooshanginejad  and Sunghwan Jung

Department of Biological and Environmental Engineering, Cornell University, Ithaca, New York 14850, USA

Ellen Longmire 

Department of Aerospace Engineering and Mechanics, University of Minnesota, Minneapolis, Minnesota 55455, USA

Sungyon Lee *

Department of Mechanical Engineering, University of Minnesota, Minneapolis, Minnesota 55455, USA



(Received 28 July 2021; revised 21 December 2021; accepted 24 May 2022; published 8 June 2022)

We experimentally investigate a millimetric armored droplet of a water-isopropyl alcohol solution sedimenting through oil and approaching a water layer at the bottom of the container. Upon reaching the oil-water interface, the droplet is shown to rupture and coalesce with the water either for low droplet densities (floating rupture) or for low oil viscosities (sinking rupture). By contrast, for sufficiently large drop density or oil viscosity, the oil covering the armored drop pinches off in the underlying water, as the armored drop continues to sink. This leads to the double encapsulation of an aqueous solution in water, which can be utilized to transport desired ingredients within a wet environment. We show that a simplified quasistatic model of a rigid sphere successfully captures the limit of the floating rupture behavior. We also rationalize the transition from the sinking rupture to oil pinch-off, by comparing the timescales of the film drainage versus sinking. Our results demonstrate that an effective Bond number and an effective Ohnesorge number are the two key dimensionless parameters that characterize the pinch-off threshold in good agreement with the experiments.

DOI: [10.1103/PhysRevFluids.7.064003](https://doi.org/10.1103/PhysRevFluids.7.064003)

I. INTRODUCTION

When particles bind to a fluid-fluid interface, the long-range capillary attraction [1] between the particles leads to the formation of so-called granular rafts [2]. For sufficiently large or heavy particles, granular rafts become unstable and form particle-*armored* droplets [3,4]. These armored drops, also known as liquid marbles [5,6], can alternatively be formed by rolling aqueous droplets on a bed of hydrophobic particles [5], or by utilizing magnetic [7] or electrical [8] forces. Liquid marbles are applicable in biochemical microreactors [9], blood typing [10], and liquid transport [11]. While a liquid marble interacting with a fluid-fluid interface has been studied under quasistatic conditions [12–15], the dynamic interaction between a liquid marble and a fluid-fluid interface poses a further complex physical picture that has not been explored.

In this study, we investigate armored drops of varying composition and density sedimenting in an immiscible liquid and approaching the interface of a liquid miscible to the droplet. While some armored drops rupture similar to a liquid drop at a miscible fluid interface, others maintain

*sungyon@umn.edu

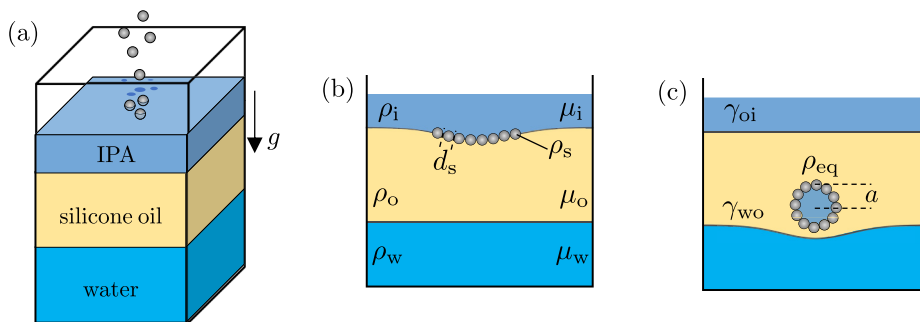


FIG. 1. (a) The 3D schematic of the stratified system where particles are slowly added from the top. (b) The schematic of the granular raft forming on an IPA-oil interface prior to the formation of the armored drop. (c) The armored drop sediments in oil and approaches the water-oil interface.

their integrity when the immiscible liquid surrounding them pinches off and allows the resulting encapsulated drop to sink, reminiscent of a solid sphere. We show that this unique combination of behaviors stems from the presence of the particle shell coupled with a dynamic fluid-fluid interface. Because of the combined features of the current system, we incorporate theories from well-established dynamics of solid spheres [16–33] and dynamics of liquid drops [34–45] at a fluid-fluid interface to characterize the different behaviors of our system.

The pinch-off behavior of an armored droplet is of particular interest, as it enables the double encapsulation of an aqueous solution in water. The double encapsulation of liquids [46–48] has been studied extensively due to the importance of stabilizing double emulsions in food [49], cosmetics [50], or drug delivery applications [51,52]. While a few studies have investigated the effects of particles in double emulsions on the submillimetric scale [53,54], particle-laden double encapsulation on the millimetric scale has not been investigated. Hence, characterizing the pinch-off behavior in the current system offers an inexpensive approach for double encapsulating liquids in a new gravity-driven regime.

The manuscript is organized as follows. In Sec. II A, we introduce our three-phase experiments and the different behaviors exhibited by the armored drops in this system. In Sec. II B, we describe our two-phase experiments and show the relationship between the properties of the individual particles and the resultant armored droplets. In Secs. III A and III B, we present a quasistatic model and scaling laws that characterize different behavioral regimes of the armored drops observed in the three-phase system. Finally, we summarize our findings and discuss future studies in Sec. IV.

II. EXPERIMENTS

A. Three-phase experiments

We conduct a series of experiments in a tank with a cross section of 12.6×12.6 cm. The tank is filled with a 5 cm layer of distilled water followed by a 5 cm layer of silicone oil with the density $\rho_o = 970 \text{ kg m}^{-3}$ and viscosity μ_o , which is varied from 0.097 to 0.97 Pa s [see Fig. 1(a)]. We add a mixture of isopropyl alcohol (IPA) and water (70% IPA by volume) on top of the oil layer; the density of the IPA mixture corresponds to $\rho_i = 850 \text{ kg m}^{-3}$. The interfacial tension between the IPA solution and silicone oil is measured to be $\gamma_{io} = 27 \text{ mN m}^{-1}$ using a pendant drop test. We then carefully deposit negatively buoyant monodisperse particles of diameter, d_s , and density, ρ_s , onto the free surface at the center of the tank to minimize wall effects. We use soda-lime glass beads (Cospheric), or ceramic-coated zirconium oxide beads (Glen Mills) with densities, $\rho_s = 2500 \text{ kg m}^{-3}$ and $\rho_s = 3800 \text{ kg m}^{-3}$, respectively, while d_s ranges from 4 to 1000 μm . For a complete range of parameters, see Appendix A.

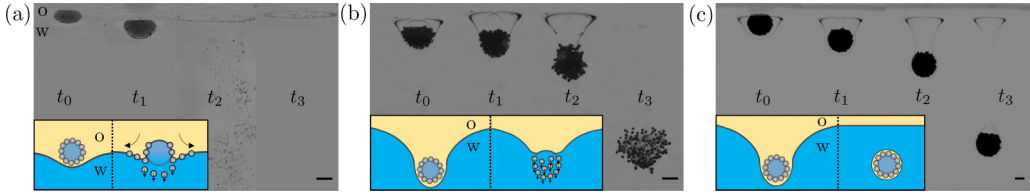


FIG. 2. Time sequential images for (a) [$d_s = 125 \mu\text{m}$, $\rho_s = 2500 \text{ kg/m}^3$, $\mu_o = 0.097 \text{ Pa s}$]: The armored drop approaches the interface ($t_0 = 0 \text{ s}$) and comes to an apparent rest ($t_1 = 0.12 \text{ s}$), until the thin film ruptures ($t_2 = 0.6 \text{ s}$). After rupture, some particles sink and some particles float and surf under a Marangoni flow ($t_3 = 0.72 \text{ s}$), as illustrated in the inset schematic. (b) [$d_s = 500 \mu\text{m}$, $\rho_s = 3800 \text{ kg/m}^3$, $\mu_o = 0.097 \text{ Pa s}$]: The interface deforms strongly ($t_0 = 0 \text{ s}$); the armored drop continues to push the interface downward into water ($t_2 = 0.02 \text{ s}$), until the oil film ruptures ($t_3 = 0.035 \text{ s}$). Then, all particles sink in water ($t_4 = 0.07 \text{ s}$), as highlighted in the inset schematic. (c) [$d_s = 350 \mu\text{m}$, $\rho_s = 2500 \text{ kg/m}^3$, $\mu_o = 0.485 \text{ Pa s}$]: The interface deforms strongly ($t_0 = 0 \text{ s}$); the armored drop continues to push the interface downward into water ($t_1 = 0.3 \text{ s}$ and $t_2 = 0.6 \text{ s}$) until the encapsulating oil pinches off ($t_4 = 0.68 \text{ s}$). The inset schematic highlights the resultant double encapsulation in the pinch-off behavior. All scale bars show 2 mm .

The particles sediment until they reach the IPA-oil interface. For the current range of d_s and ρ_s , each particle comes to rest at the oil-IPA interface as the capillary force on the particle dominates the gravitational and buoyant forces. The centimetric-scale granular raft that forms due to the capillary attraction between floating particles subsequently deforms the interface under gravitational effects. Once the granular raft grows large enough, it becomes unstable, which results in the encapsulation of particle-coated IPA in the form of an armored drop in silicone oil [3].

Once the armored drop forms at the IPA-oil interface, it sediments towards the oil-water interface, as illustrated in Figs. 1(b) and 1(c). The thickness of the silicone oil layer is chosen so that all tested armored drops reach their terminal velocity before reaching the oil-water interface. Drops covered with smaller or lighter particles settle slowly while deforming the interface minimally. For these armored drops, the deformed interface comes to rest macroscopically shortly after the deformation begins, as indicated in time sequential snapshots of Fig. 2(a). However, the armored drop continues to slowly sediment and thin the film between the armored drop and the interface until the long range van der Waals forces dominate. At this point, water bridges through the particle-armor, and the particle-armor ruptures. Upon rupture, the particles below the free surface immerse in water, while the particles above the free surface stay trapped on the oil-water interface under capillary forces. Under this behavior, some particles float on the interface, while others sink as illustrated in the inset of Fig. 2(a). Notably, the floating particles undergo a radially outward Marangoni flow due to the release of the IPA inside the armored drop [55]. We refer to this behavior as *floating rupture*.

For armored drops with larger or heavier particles, two distinct behaviors are observed: rupture and pinch-off. For both behaviors, the armored drop continuously deforms the interface and approaches the pinch-off, distinct from the floating rupture scenario. However, for lower viscosities of silicone oil, the thin film between the armored drop and the interface drains faster than the time it takes for the pinch-off of the encapsulating oil, leading to the film rupture [see Fig. 2(b)]. We refer to this behavior as *sinking rupture*. In this regime, all particles become immersed in water and sink as indicated in the inset schematic of Fig. 2(b) [55]. On the contrary, for silicone oil with higher viscosities, the oil filament encapsulating the armored drop pinches off before the thin film drains completely, as shown in Fig. 2(c) [55]. We refer to this behavior as *pinch-off*. Under this behavior, IPA is double encapsulated in water, as illustrated in the inset of Fig. 2(c). The experimental movies of all three droplet behaviors are included as Supplemental Material [55].

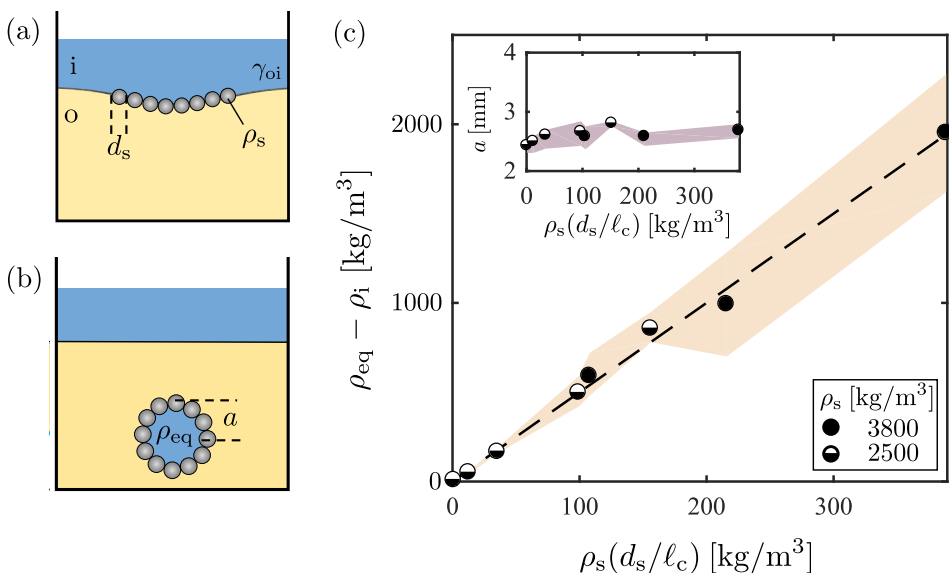


FIG. 3. Schematics for two-phase experiments (a) before and (b) after formation of the armored drop. (c) The armored drop equivalent density, $\rho_{\text{eq}} - \rho_i$, as a function of $\rho_s d_s / \ell_c$ for varying particle sizes, $d_s = 4\text{--}1000\ \mu\text{m}$, and particle densities, $\rho_s = 2500\ \text{kg m}^{-3}$ (half-filled) or $\rho_s = 3800\ \text{kg m}^{-3}$ (filled). The dashed line corresponds to the total mass calculation with particle packing fraction, $\phi = 0.76$. Inset: The armored drop equivalent radius, a , for varying $\rho_s d_s / \ell_c$.

B. Two-phase experiments

To characterize the equivalent radius, a , and density, ρ_{eq} , of the armored drop systematically, we perform a series of two-layer experiments. As indicated in the schematics in Fig. 3(a), we examine different particle densities and particle sizes in the same tank filled with different viscosities of silicone oil, $\mu_o = 0.291, 0.485, \text{ and } 0.97\ \text{Pa s}$ and a thin layer of the 70% IPA solution on top. We find ρ_{eq} by measuring the terminal settling velocity, V , and approximating it as the Stokes settling velocity, or $V \approx 2(\rho_{\text{eq}} - \rho_o)ga^2 / (9\mu_o)$. Figure 3(c) shows $\rho_{\text{eq}} - \rho_i$ for varying $\rho_s d_s / \ell_c$, where $\ell_c = \sqrt{\gamma_{oi}(\rho_o - \rho_i)^{-1}g^{-1}}$ denotes the capillary length for the silicone oil and IPA. If we assume that particles are half immersed in the drop and half in the continuous phase, then the total mass calculation for a monolayer armored drop yields $\rho_{\text{eq}} - \rho_i = 2\phi\rho_s d_s / a$, where ϕ denotes the particle packing fraction. As a varies negligibly between 2.4 and 2.8 mm under the current parameter range [see the inset of Fig. 3(c)], $\rho_{\text{eq}} - \rho_i$ is shown to increase linearly with increasing $\rho_s d_s$, as plotted in Fig. 3(c). The linear fit for ρ_{eq} corresponds to $\phi = 0.76$, which is very close to the packing volume fraction in the granular raft prior to destabilization [4]. Details of how we measure ϕ is provided in Appendix B.

III. MODEL

A. Quasistatic model

Inspired by the behavior of a solid sphere at a fluid-fluid interface which either *floats* or *sinks*, we apply a quasistatic force balance on an armored drop. In the manner of Refs. [25,30], the drop is approximated as a rigid sphere (density ρ_{eq}) at rest on the oil-water interface with a contact angle θ . We note that in the case of the armored drop, there is a thin film between the armored drop and the interface, therefore, all force balance arguments apply to a negligibly larger control volume, while θ corresponds to the apparent contact angle as depicted in Fig. 4(a). The particle wettability has some importance on the IPA-oil interface to enable the formation of a granular raft that eventually

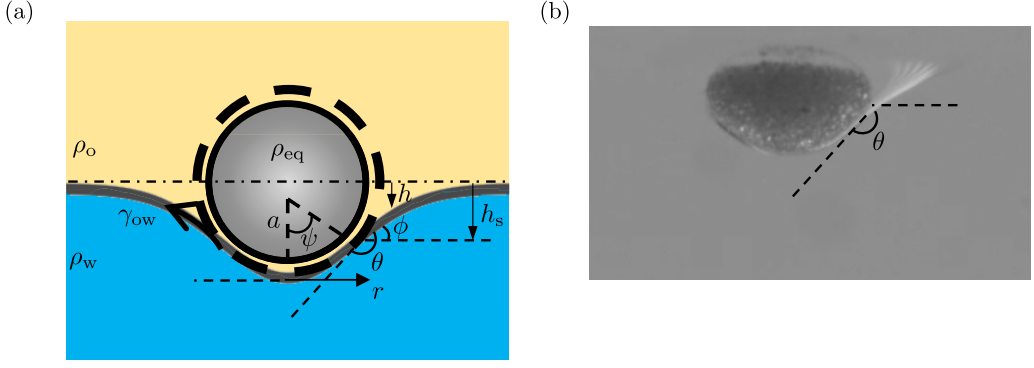


FIG. 4. (a) Schematics of a sphere in equilibrium at a fluid-fluid interface. (b) An armored drop [$\rho_s = 2500 \text{ kg m}^{-3}$, $d_s = 125 \text{ }\mu\text{m}$, $\mu_o = 0.485 \text{ Pa s}$] before the onset of rupture.

destabilizes into an armored drop. However, armored drops made with glass beads (contact angle $\leq 15^\circ$ [56]) and those made with zirconia beads (contact angle $\sim 101^\circ$ [57]) do not exhibit noticeable differences at the oil-water interface. We speculate that the wettability of particles will ultimately be important in initiating the rupture event microscopically. However, such effects are out of scope of the current study and may be considered in the future.

Under quasistatic assumptions, the sphere deforms the interface below it. As depicted in Fig. 4(a), the interface gets separated from the sphere at an angle ψ from the centerline with a slope angle ϕ with distance h_s from the free surface. If we normalize the parameters with the capillary length, $\ell_{c,ow} = \sqrt{\gamma_{ow}(\rho_w - \rho_o)^{-1}g^{-1}}$, then balancing the gravitational force with the buoyancy and surface tension forces yields

$$\frac{4}{3}\Gamma R^{*3} = 2R^* \sin \psi \sin \phi + \frac{2}{3}R^{*3} - R^{*3} \cos \psi + \frac{1}{3}R^{*3} \cos^3 \psi - R^{*2}h_s^* \sin^2 \psi, \quad (1)$$

where $\Gamma = (\rho_{eq} - \rho_o)/(\rho_w - \rho_o)$, $R^* = a/\ell_{c,ow}$, and $h_s^* = h_s/\ell_{c,ow}$. The interface profile is determined by the Young-Laplace equation,

$$\frac{h^{*''}}{1 + h^{*'}{}^2} + \frac{h^{*'}}{r^*} - h^* \sqrt{1 + h^{*'}{}^2} = 0, \quad (2)$$

where the asterisk denotes dimensionless parameters normalized by $\ell_{c,ow}$, and the prime denotes the derivative with respect to r^* . We solve Eqs. (1) and (2), subject to the boundary conditions $h^{*'}(R^* \sin \psi) = \tan \phi$ and $h^*(\infty) = 0$, along with the geometrical constraint of $\theta - \phi + \psi = \pi$. Then, for varying ϕ , we find the maximum value of Γ that yields an equilibrium state.

The sphere floats when the solution for the interfacial shape exists under the quasistatic force balance, but sinks when no equilibrium solution exists [25]. If the equilibrium solution exists for a solid sphere, then we expect the equivalent armored drop to exhibit the floating rupture behavior, as it is the only case where the interface comes to a macroscopic equilibrium before the oil film ruptures. However, if the quasistatic analysis yields sinking, then the armored drop may exhibit either sinking rupture or pinch-off. Figure 5 summarizes the three distinct behaviors in a phase diagram for the dimensionless density, Γ , as a function of Bond number, $\text{Bo} = (\rho_w - \rho_o)ga^2/\gamma_{wo}$. We consider a range of θ in the model and find the corresponding sinking threshold. Notably, the transition from floating rupture to either sinking rupture or pinch-off is well predicted by the lower and upper bounds of $\theta = \pi/2$ (dotted-dashed line) and $\theta = 3\pi/5$ (dashed line), shown in Fig. 5, respectively. While we cannot measure θ precisely, our experimental images strongly suggest that $\theta > \pi/2$ for all floating rupture cases, as the oil-water interface is shown to deviate from the lower half of the droplet as illustrated in Fig. 4(b). Therefore, $\pi/2 < \theta < 3\pi/5$ is in good qualitative agreement with the experiments.

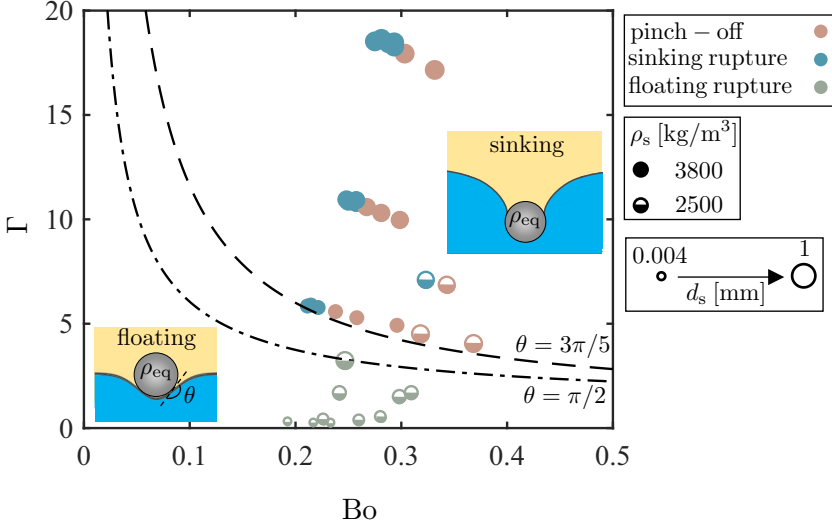


FIG. 5. The phase diagram showing Bo vs Γ for the particle density, $\rho_s = 2500 \text{ kg/m}^3$ (half-filled), or $\rho_s = 3800 \text{ kg/m}^3$ (filled), and varying particle sizes (corresponding varying symbol sizes). Error bars are smaller than symbol sizes. The dotted-dashed line and the dashed line correspond to the upper bounds (i.e., Γ_{\max}) of the floating behavior from the quasistatic force balance [25,30] for $\theta = \pi/2$ and $\theta = 3\pi/5$, respectively.

For $Bo \ll 1$, Eq. (1) yields

$$\Gamma Bo \approx 3(1 - \cos \theta)/4. \quad (3)$$

ΓBo is an important dimensionless parameter as it considers the effects of both a and ρ_{eq} . Therefore, we refer to ΓBo as the effective Bond number, $Bo_{\text{eff}} = (\rho_{\text{eq}} - \rho_o)ga^2/\gamma_{wo}$. Note that we change Bo_{eff} in our experiments mainly by varying ρ_{eq} through ρ_s and d_s .

B. Scaling laws

As shown in Fig. 5, the quasistatic force balance does not differentiate sinking rupture from pinch-off. This implies that in both cases, oil surrounding the armored drop approaches pinch-off. Hence, we can determine whether or not the film ruptures before pinch-off by comparing the timescale of sinking with that of the film drainage. The settling velocity in our experiments ranges from 1 to 10 cm/s, with the corresponding Reynolds number Re ranging from 0.05 to 2.5. However, all the cases of $Re > 1$ belong to $\mu_o = 0.097 \text{ Pa}\cdot\text{s}$, where all the armored drops exhibit floating rupture. For all the other cases, $Re < 0.3$, including the cases near the transition from sinking rupture to pinch off. Therefore, for simplicity, we assume $Re \ll 1$ to model that transition.

To find the sinking timescale, we consider the early stage of armored drop sinking in water while encapsulated in an elongating oil filament as depicted in Fig. 6. We simplify the armored drop and the thin oil film encapsulating the drop as a rigid sphere of radius, a , and density, ρ_{eq} , that is sinking in water with velocity V . Then, the force balance on the control volume (a dashed circle in Fig. 6) yields

$$\rho_{\text{eq}}a^3 \frac{dV}{dt} \sim F_g - F_b - F_\gamma - F_{\text{drag}}, \quad (4)$$

where the right-hand side denotes the gravitational force, the buoyant force, the capillary force, and the drag force on the control volume, respectively.

The drag force is estimated as a Stokes drag on a sphere sinking in water, $F_{\text{drag}} \sim \mu_w Va$. Then, the force balance becomes

$$\rho_{\text{eq}}a^3 \frac{dV}{dt} \sim (\rho_{\text{eq}} - \rho_w)a^3 g - \gamma_{wo}a - \mu_w Va, \quad (5)$$

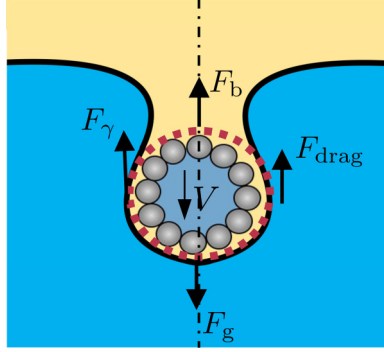


FIG. 6. Schematics of a sinking armored drop approaching pinch-off.

where $dV/dt \sim a/\tau_s^2$, and τ_s denotes the sinking timescale. As the armored drop approaches and deforms the oil-water interface, it decelerates by a small amount. Nevertheless, its velocity still scales as the terminal settling velocity in oil at the early stage of sinking, so that $F_{\text{drag}} \sim (\rho_{\text{eq}} - \rho_o)a^3 g \mu_w / \mu_o$. In addition, as $\mu_w / \mu_o \ll 1$ for our current range of parameters, $F_{\text{drag}} \ll F_g$, which allows us to neglect the drag force term in Eq. (5). Furthermore, we note that $\text{Bo} \ll \text{Bo}_{\text{eff}}$ for both sinking rupture and pinch-off behaviors in our experiments. Therefore, Eq. (5) simplifies to

$$\tau_s^{-2} \sim \frac{\gamma_{\text{wo}}}{\rho_{\text{eq}} a^3} (\text{Bo}_{\text{eff}} - 1). \quad (6)$$

Next, we discuss the lubrication model for finding the film drainage timescale inspired by Ref. [34]. To find the timescale of the film drainage, we consider the simplified case of a rigid sphere approaching a rigid planar surface. For a sinking sphere with velocity, V , pressure increases inside the film below the sinking sphere. This pressure build-up drives a flow that drains the film and thins the gap as shown in Fig. 7. We consider the translation of a rigid sphere with density ρ_{eq} and radius a approaching a shear-free planar boundary with a relative velocity, v , when the distance between the sphere and the boundary along the centerline, h_0 , is much smaller than the radius (i.e., $h_0 \ll a$). For consistency, the fluid density and viscosity are denoted as ρ_o and μ_o , respectively. Then, under lubrication approximations, the flow inside the gap in cylindrical coordinate yields

$$u_r = \frac{1}{2\mu_o} \frac{\partial p}{\partial r} (z^2 - h^2), \quad (7)$$

where $p(r, t)$ is the pressure inside the gap.

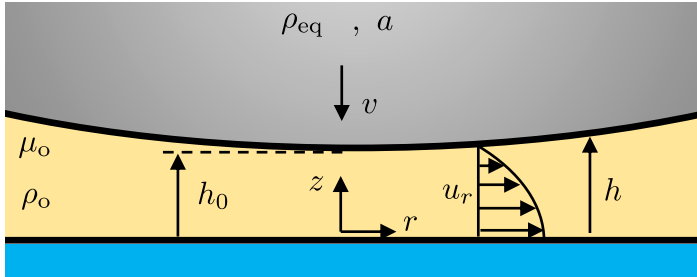


FIG. 7. The schematic of a sphere settling toward a shear free planar boundary.

Also, integrating the continuity equation, $(1/r)\partial_r(ru_r) + \partial_z u_z = 0$, across the gap yields

$$\int_0^{h(r,t)} \frac{1}{r} \frac{\partial(ru_r)}{\partial r} dz + v(t) = 0. \quad (8)$$

By combining Eq. (7) with Eq. (8), and after some algebra, we obtain

$$\frac{\partial}{\partial r} \left(rh^3 \frac{\partial p}{\partial r} \right) = 3\mu_o v r \Rightarrow h^3 \frac{\partial p}{\partial r} = \frac{3}{2} \mu_o v r. \quad (9)$$

The Taylor expansion of the film thickness near the center where the pressure gradient is dominant corresponds to $h(r, t) = h_0(t) + r^2/2a$. Therefore, integrating Eq. (9) with respect to r yields

$$p(r, t) = p_0 - \frac{3\mu_o v a}{4(h_0 + \frac{r^2}{2a})^2}. \quad (10)$$

From Eq. (10), we can calculate the resistive force exerted on the sphere by the pressure build-up inside the film,

$$F = -2\pi \int_0^a (p - p_0)r dr \approx -\frac{3}{2} \frac{\mu_o v a^2}{2h_0}, \quad (11)$$

where $h_0 \ll a$. As $v < 0$, the resistive force is positive in the z direction. Finally, the resistive force balances the gravitational and buoyant forces in the low Re regime,

$$\frac{4}{3} \pi a^3 \Delta \rho g = -\frac{3}{2} \frac{\mu_o v a^2}{h_0(t)} \Rightarrow \frac{v}{h_0} = -\frac{8}{9} \frac{\Delta \rho g a}{\mu_o}, \quad (12)$$

where $\Delta \rho = \rho_{eq} - \rho_o$. The left-hand side of Eq. (12) represents the inverse of the film drainage timescale, τ_d . Therefore, we conclude $\tau_d \sim \mu_o/(\Delta \rho g a)$.

By comparing the film drainage time and the sinking time, we obtain

$$\frac{\tau_d^2}{\tau_s^2} \sim \text{Oh}^2 \left(\frac{\rho_o}{\rho_{eq}} \right) \text{Bo}_{\text{eff}}^{-2} (\text{Bo}_{\text{eff}} - 1), \quad (13)$$

where $\text{Oh} = \mu_o/\sqrt{\gamma_{wo}\rho_o a}$ denotes the Ohnesorge number. The pinch-off condition, $\tau_d/\tau_s > 1$, further reduces to

$$\text{Oh}_{\text{eff}} > \frac{\text{Bo}_{\text{eff}}}{\sqrt{\text{Bo}_{\text{eff}} - 1}}, \quad (14)$$

where $\text{Oh}_{\text{eff}} = \mu_o/\sqrt{\gamma_{wo}\rho_{eq} a}$. Notably, for $\text{Bo}_{\text{eff}} \gg 1$ this simplifies to $\text{Oh}_{\text{eff}} > \text{Bo}_{\text{eff}}^{1/2}$. Figure 8 shows the three behaviors of the armored drop for varying Oh_{eff} as a function of Bo_{eff} . The solid line shows the scaling of Eq. (14) for the transition from sinking rupture to pinch-off, which is in good qualitative agreement with the experiments.

As shown in Fig. 8, the pinch-off occurs only for $\text{Bo}_{\text{eff}} \gtrsim 1$, as all armored drops with $\text{Bo}_{\text{eff}} < 1$ undergo floating rupture. Notably, the two vertical lines in Fig. 8 correspond to Bo_{eff} scaling for the limit of floating rupture when $\theta = \pi/2$ (dotted dashed) and $\theta = 3\pi/5$ (dashed), respectively. In addition, when $\text{Bo}_{\text{eff}} \gtrsim 1$, the minimum value of Oh_{eff} required for pinch-off increases weakly with Bo_{eff} . Note that Oh_{eff} at a given Bo_{eff} is primarily varied in our experiments by changing μ_o . In other words, for a larger particle density or particle size (i.e., increasing Bo_{eff}), a larger oil viscosity is required to slow down the drainage rate before pinch-off.

IV. SUMMARY AND DISCUSSION

We present a system of three fluid layers where a granular raft at the first interface between oil and IPA leads to the formation of an armored drop. The resultant droplet encapsulates IPA and sinks in oil toward the second interface between water and oil. We demonstrate that the dynamic

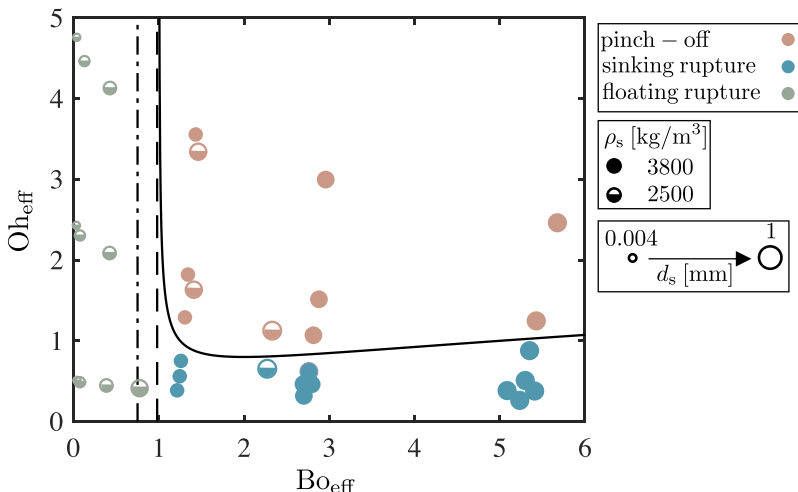


FIG. 8. The phase diagram showing Bo_{eff} vs Oh_{eff} for the particle density, $\rho_s = 2500 \text{ kg/m}^3$ (half-filled), or $\rho_s = 3800 \text{ kg/m}^3$ (filled), and varying particle sizes (corresponding varying symbol sizes). Error bars are smaller than the symbol sizes. The dotted-dashed line and the dashed line correspond to $Bo_{\text{eff}} \approx 3(1 - \cos\theta)/4$ for $\theta = \pi/2$, and $\theta = 3\pi/5$, respectively. The solid line shows $Oh_{\text{eff}} = 0.4 Bo_{\text{eff}}/\sqrt{Bo_{\text{eff}} - 1}$.

interaction between the sinking armored drop and the oil-water interface can result in three different behaviors: floating rupture, sinking rupture, or pinch-off. We first show that Γ and Bo are the key independent parameters to characterize the transition from the floating rupture regime to the other two regimes. In addition, we incorporate scaling arguments to show that Oh_{eff} and Bo_{eff} are the key parameters to characterize the transition from the sinking rupture regime to the pinch-off regime. The transition from sinking rupture to pinch-off is shown to scale as $Oh_{\text{eff}} \sim Bo_{\text{eff}}/\sqrt{Bo_{\text{eff}} - 1}$, which yields $Oh_{\text{eff}} \sim Bo_{\text{eff}}^{1/2}$ in the limit of $Bo_{\text{eff}} \gg 1$. Therefore, since $Bo_{\text{eff}} = \Gamma Bo$, the complete phase separation requires three independent parameters (i.e., Bo , Γ , and Oh_{eff}).

The current system offers a gravity-driven method to generate double encapsulated liquids on a millimetric scale, by using granular rafts coupled with a fluid-fluid interface. As indicated in Fig. 8, either large Bo_{eff} or large Oh_{eff} is required to achieve double encapsulation (i.e., pinch-off). Notably, the size of the armored droplet appears constant in the current setup, while its effective density is shown to vary linearly with $\rho_s d_s$. Hence, the density of the double encapsulated drops can be controlled with the choice of particle properties as well as encapsulated fluid properties. While our scaling argument for the transition from sinking rupture to pinch-off is in good agreement with the experiments, we acknowledge that the current experimental setting only allows for the partial validation of the individual parameters included in Oh_{eff} and Bo_{eff} . Additional experiments with different fluid systems are required to validate the universality of our model. For instance, exploring the effect of surfactants at the water-oil interface is recommended as it increases both Bo_{eff} and Oh_{eff} , which will presumably expand the range of pinch-off regime for varying compositions of the armored drop. We also note that applying additional body forces such as a centrifugal force can expand the range of armored drop sizes to a submillimeter scale [58] while maintaining $Bo_{\text{eff}} > 1$ and $Oh_{\text{eff}} > 1$ required for double-encapsulation.

ACKNOWLEDGMENTS

We thank H. A. Stone and M. Abkarian for fruitful discussions. This work was supported in part by the NSF (Grants No. CBET-1605947 and No. CBET-2032354).

APPENDIX A: PARAMETER SPACE IN EXPERIMENTS

Table I includes the complete list of the particles (density and diameter) and silicone oil (viscosity) used in the experiments. It also lists the corresponding behavior of the armored droplet for the given combination of particles and oils used. Table II comprises the particle diameters and the corresponding symbol sizes used in Figs. 3 and 4.

TABLE I. Different parameters tested in the experiments presented in Figs. 3 and 4.

particles \ oil viscosity	0.096 Pa.s	0.143 Pa.s	0.192 Pa.s	0.34 Pa.s	0.483 Pa.s	0.97 Pa.s
$\rho_s = 2500 \text{ kg/m}^3, d_s = 3 - 6\mu\text{m}$	floating rupture				floating rupture	floating rupture
$\rho_s = 2500 \text{ kg/m}^3, d_s = 30 - 60\mu\text{m}$	floating rupture				floating rupture	floating rupture
$\rho_s = 2500 \text{ kg/m}^3, d_s = 100 - 150\mu\text{m}$	floating rupture				floating rupture	floating rupture
$\rho_s = 2500 \text{ kg/m}^3, d_s = 300 - 400\mu\text{m}$	floating rupture				pinch - off	pinch - off
$\rho_s = 2500 \text{ kg/m}^3, d_s = 500 - 600\mu\text{m}$			sinking rupture	pinch - off		
$\rho_s = 3800 \text{ kg/m}^3, d_s = 200 - 300\mu\text{m}$	sinking rupture	sinking rupture	sinking rupture	pinch - off	pinch - off	pinch - off
$\rho_s = 3800 \text{ kg/m}^3, d_s = 400 - 600\mu\text{m}$	sinking rupture	sinking rupture	sinking rupture	pinch - off	pinch - off	pinch - off
$\rho_s = 3800 \text{ kg/m}^3, d_s = 800 - 1000\mu\text{m}$	sinking rupture	sinking rupture	sinking rupture	sinking rupture	pinch - off	pinch - off

TABLE II. Different parameters tested in the experiments presented in Figs. 3 and 4.

$d_s [\mu\text{m}]$	3 - 6	30 - 60	100 - 150	200 - 300	300 - 400	400 - 600	500 - 600	800 - 1000
symbol size	•	•	◦	◦	◦	◦	◦	◦

APPENDIX B: ARMORED DROP DENSITY MEASUREMENTS

To measure the settling velocity of the armored drops, we perform MATLAB image processing to track the front (i.e., lowest) point on the armored drop. We then extract the velocity when it reaches a plateau.

We measure the equivalent density, ρ_{eq} , of the armored drop via two methods. First, we calculate ρ_{eq} by plugging in the measured terminal velocity into the expression for the Stokes terminal velocity. Second, we perform image processing to extract the shape of the falling armored drop shape as shown in Fig. 9. We then measure the area covered by the solid particles, A_s , by assuming an axisymmetric shape for the falling armored drop:

$$A_s = \int_0^{H_s} 2\pi \left[R(z) - \frac{d_s}{2} \right] dz, \quad (\text{B1})$$

where H_s denotes the height of the drop that is covered by the particles as shown in Fig. 9. By assuming a monolayer of particles armor the drop, the total number of particles can be approximated as $n_s = 4\phi A_s / (\pi d_s^2)$, where ϕ is the surface packing fraction of particles. Therefore, the mass of particles yields $m_s = (2/3)\phi A_s \rho_s d_s$.

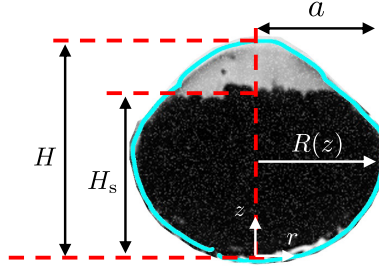


FIG. 9. A snapshot of an armored drop sinking in oil.

Next, we measure the total volume of the fluid encapsulated in the armored drop,

$$V_f = \int_0^{H_s} \pi \left(R(z) - \frac{d_s}{2} \right)^2 dz + \int_{H_s}^H \pi R^2(z) dz. \quad (\text{B2})$$

Here, H denotes the total height of the armored drop as shown in Fig. 9. Finally, the total mass of the armored drop, m , yields

$$m = \frac{2}{3} \phi A_s \rho_s d_s + \rho_f V_f. \quad (\text{B3})$$

Hence, the equivalent density of the armored drop can be approximated as $\rho_{\text{eq}} = (2/3)\phi A_s \rho_s d_s / V_f + \rho_f$. Note that the data presented in Fig. 3(c) is extracted from the first method (i.e., using steady settling velocity). For $\phi = 0.76$, we get a match with the data presented in Fig. 3(c) with less than 2% error by using the second method.

-
- [1] D. Vella and L. Mahadevan, The ‘‘cheerios effect,’’ *Am. J. Phys.* **73**, 817 (2005).
 - [2] P. Cicuta and D. Vella, Granular Character of Particle Rafts, *Phys. Rev. Lett.* **102**, 138302 (2009).
 - [3] M. Abkarian, S. Protière, J. M. Aristoff, and H. A. Stone, Gravity-induced encapsulation of liquids by destabilization of granular rafts, *Nat. Commun.* **4**, 1895 (2013).
 - [4] S. Protière, C. Josserand, J. M. Aristoff, H. A. Stone, and M. Abkarian, Sinking a Granular Raft, *Phys. Rev. Lett.* **118**, 108001 (2017).
 - [5] P. Aussillous and D. Quéré, Liquid marbles, *Nature (London)* **411**, 924 (2001).
 - [6] N. Pike, D. Richard, W. Foster, and L. Mahadevan, How aphids lose their marbles, *Proc. R. Soc. Lond. B* **269**, 1211 (2002).
 - [7] Y. Zhao, J. Fang, H. Wang, X. Wang, and T. Lin, Magnetic liquid marbles: Manipulation of liquid droplets using highly hydrophobic Fe_3O_4 nanoparticles, *Adv. Mater.* **22**, 707 (2010).
 - [8] P. Aussillous and D. Quéré, Properties of liquid marbles, *Proc. Roy. Soc. A: Math. Phys. Eng. Sci.* **462**, 973 (2006).
 - [9] X. Tang, S. Tang, V. Sivan, W. Zhang, A. Mitchell, K. Kalantar-zadeh, and K. Khoshmanesh, Photochemically induced motion of liquid metal marbles, *Appl. Phys. Lett.* **103**, 174104 (2013).
 - [10] T. Arbatan, L. Li, J. Tian, and W. Shen, Liquid marbles as micro-bioreactors for rapid blood typing, *Adv. Healthcare Mater.* **1**, 80 (2012).
 - [11] E. Jambon-Puillet, C. Josserand, and S. Protière, Drops floating on granular rafts: A tool for liquid transport and delivery, *Langmuir* **34**, 4437 (2018).
 - [12] G. McHale and M. I. Newton, Liquid marbles: Principles and applications, *Soft Matter* **7**, 5473 (2011).
 - [13] G. McHale and M. I. Newton, Liquid marbles: Topical context within soft matter and recent progress, *Soft Matter* **11**, 2530 (2015).
 - [14] C. H. Ooi, C. Plackowski, A. V. Nguyen, R. K. Vadivelu, J. A. St. John, D. V. Dao, and N. Nguyen, Floating mechanism of a small liquid marble, *Sci. Rep.* **6**, 21777 (2016).

- [15] H. Kawashima, M. Paven, H. Mayama, H. Butt, Y. Nakamura, and S. Fujii, Transfer of materials from water to solid surfaces using liquid marbles, *ACS Appl. Mater. Interfaces* **9**, 33351 (2017).
- [16] S. Hartland, The profile of the draining film between a rigid sphere and a deformable fluid-liquid interface, *Chem. Eng. Sci.* **24**, 987 (1969).
- [17] H. C. Maru, D. T. Wasan, and R. C. Kintner, Behavior of a rigid sphere at a liquid-liquid interface, *Chem. Eng. Sci.* **26**, 1615 (1971).
- [18] A. Scheludko, B. V. Toshev, and D. T. Bojadjev, Attachment of particles to a liquid surface (capillary theory of flotation), *J. Chem. Soc., Faraday Trans. 1* **72**, 2815 (1976).
- [19] A. V. Rapacchietta, A. W. Neumann, and S. N. Omenyi, Force and free-energy analyses of small particles at fluid interfaces: I. Cylinders, *J. Colloid Interface Sci.* **59**, 541 (1977).
- [20] C. Berdan II and L.G Leal, Motion of a sphere in the presence of a deformable interface: I. Perturbation of the interface from flat: The effects on drag and torque, *J. Colloid Interface Sci.* **87**, 62 (1982).
- [21] S. H. Lee and L. G. Leal, The motion of a sphere in the presence of a deformable interface: II. A numerical study of the translation of a sphere normal to an interface, *J. Colloid Interface Sci.* **87**, 81 (1982).
- [22] A. S. Geller, S. H. Lee, and L. G. Leal, The creeping motion of a spherical particle normal to a deformable interface, *J. Fluid Mech.* **169**, 27 (1986).
- [23] J. B. Keller, Surface tension force on a partly submerged body, *Phys. Fluids* **10**, 3009 (1998).
- [24] D. Vella, P. D. Metcalfe, and R. J. Whittaker, Equilibrium conditions for the floating of multiple interfacial objects, *J. Fluid Mech.* **549**, 215 (2006).
- [25] D. Vella, D. Lee, and H. Kim, The load supported by small floating objects, *Langmuir* **22**, 5979 (2006).
- [26] D. Lee and H. Kim, Sinking of small sphere at low Reynolds number through interface, *Phys. Fluids* **23**, 072104 (2011).
- [27] C. Pozrikidis, A floating prolate spheroid, *J. Colloid Interface Sci.* **364**, 248 (2011).
- [28] R. Camassa, S. Khatri, R. M. McLaughlin, J. C. Prairie, B. L. White, and S. Yu, Retention and entrainment effects: Experiments and theory for porous spheres settling in sharply stratified fluids, *Phys. Fluids* **25**, 081701 (2013).
- [29] D. Vella, Floating versus sinking, *Annu. Rev. Fluid Mech.* **47**, 115 (2015).
- [30] J. Pierson and J. Magnaudet, Inertial settling of a sphere through an interface. Part 1. From sphere flotation to wake fragmentation, *J. Fluid Mech.* **835**, 762 (2018).
- [31] J. Pierson and J. Magnaudet, Inertial settling of a sphere through an interface. Part 2. Sphere and tail dynamics, *J. Fluid Mech.* **835**, 808 (2018).
- [32] J. Magnaudet and M. J. Mercier, Particles, drops, and bubbles moving across sharp interfaces and stratified layers, *Annu. Rev. Fluid Mech.* **52**, 61 (2020).
- [33] P. A. Jarvis, H. M. Mader, H. E. Huppert, K. V. Cashman, and J. D. Blundy, Experiments on the low-Reynolds-number settling of a sphere through a fluid interface, *Phys. Rev. Fluids* **4**, 024003 (2019).
- [34] G. E. Charles and S. G. Mason, The coalescence of liquid drops with flat liquid/liquid interfaces, *J. Colloid Sci.* **15**, 236 (1960).
- [35] A. F. Jones and S. D. R. Wilson, The film drainage problem in droplet coalescence, *J. Fluid Mech.* **87**, 263 (1978).
- [36] J. Chen, P. S. Hahn, and J. C. Slattery, Coalescence time for a small drop or bubble at a fluid-fluid interface, *AIChE J.* **30**, 622 (1984).
- [37] P. S. Hahn, J. Chen, and J. C. Slattery, Effects of London-van der Waals forces on the thinning and rupture of a dimpled liquid film as a small drop or bubble approaches a fluid-fluid interface, *AIChE J.* **31**, 2026 (1985).
- [38] B. K. Chi and L. G. Leal, A theoretical study of the motion of a viscous drop toward a fluid interface at low Reynolds number, *J. Fluid Mech.* **201**, 123 (1989).
- [39] S. G. Yiantsios and R. H. Davis, On the buoyancy-driven motion of a drop towards a rigid surface or a deformable interface, *J. Fluid Mech.* **217**, 547 (1990).
- [40] M. Manga and H. A. Stone, Low Reynolds number motion of bubbles, drops and rigid spheres through fluid-fluid interfaces, *J. Fluid Mech.* **287**, 279 (1995).
- [41] Z. Mohamed-Kassim and E. K. Longmire, Drop impact on a liquid-liquid interface, *Phys. Fluids* **15**, 3263 (2003).

- [42] Z. Mohamed-Kassim and E. K. Longmire, Drop coalescence through a liquid/liquid interface, *Phys. Fluids* **16**, 2170 (2004).
- [43] F. Blanchette and T. P. Bigioni, Dynamics of drop coalescence at fluid interfaces, *J. Fluid Mech.* **620**, 333 (2009).
- [44] C. Ortiz-Dueñas, J. Kim, and E. K. Longmire, Investigation of liquid–liquid drop coalescence using tomographic PIV, *Exp. Fluids* **49**, 111 (2010).
- [45] H. P. Kavehpour, Coalescence of drops, *Annu. Rev. Fluid Mech.* **47**, 245 (2015).
- [46] M. Kanouni, H. L. Rosano, and N. Naouli, Preparation of a stable double emulsion ($w_1/o/w_2$): role of the interfacial films on the stability of the system, *Adv. Colloid Interface Sci.* **99**, 229 (2002).
- [47] A. S. Utada, E. Lorenceau, D. R. Link, P. D. Kaplan, H. A. Stone, and D. A. Weitz, Monodisperse double emulsions generated from a microcapillary device, *Science* **308**, 537 (2005).
- [48] J. G. Xu, R. Chen, Y. Wang, and G. Luo, Controllable gas/liquid/liquid double emulsions in a dual-coaxial microfluidic device, *Lab Chip* **12**, 2029 (2012).
- [49] G. Muschiolik and E. Dickinson, Double emulsions relevant to food systems: Preparation, stability, and applications, *Comp. Rev. Food Sci. Food Safety* **16**, 532 (2017).
- [50] N. Garti and C. Bisperink, Double emulsions: Progress and applications, *Curr. Opin. Colloid Interface Sci.* **3**, 657 (1998).
- [51] S. Cohen, T. Yoshioka, M. Lucarelli, L. H. Hwang, and R. Langer, Controlled delivery systems for proteins based on poly (lactic/glycolic acid) microspheres, *Pharmaceut. Res.* **8**, 713 (1991).
- [52] M. Iqbal, N. Zafar, H. Fessi, and A. Elaissari, Double emulsion solvent evaporation techniques used for drug encapsulation, *Int. J. Pharmaceut.* **496**, 173 (2015).
- [53] B. J. Sun, H. C. Shum, C. Holtze, and D. A. Weitz, Microfluidic melt emulsification for encapsulation and release of actives, *ACS Appl. Mater. Interfaces* **2**, 3411 (2010).
- [54] H. Lamba, K. Sathish, and L. Sabikhi, Double emulsions: Emerging delivery system for plant bioactives, *Food Bioprocess Technol.* **8**, 709 (2015).
- [55] See Supplemental Material at <http://link.aps.org/supplemental/10.1103/PhysRevFluids.7.064003> for the full parameter space in the experiments, movies showing different behaviors of the armored drop presented in Fig. 2, and details concerning the model.
- [56] M. Wei, R. S. Bowman, J. L. Wilson, and N. R. Morrow, Wetting properties and stability of silane-treated glass exposed to water, air, and oil, *J. Colloid Interface Sci.* **157**, 154 (1993).
- [57] U. Patel, K. Patel, K. Chauhan, A. Chawla, and S. Rawal, Investigation of various properties for zirconium oxide films synthesized by sputtering, *Procedia Technol.* **23**, 336 (2016).
- [58] M. Abkarian, E. Loiseau, and G. Massiera, Continuous droplet interface crossing encapsulation (CDICE) for high throughput monodisperse vesicle design, *Soft Matter* **7**, 4610 (2011).